COMMUNICATIONS IN SCIENCE AND TECHNOLOGY
Homepage: cst.kipmi.or.id

Annealing temperature modify of crystalline structure, magnetic properties and antibacterial performance in nickel substituted cobalt ferrite nanoparticles utilizing natural-fine-sediment

Laksmita Farah Bestari, Lathifah Iqlimatussholihah, Nurdiyantoro Putra Prasetya, Kusumandari, Utari, Riyatun, Budi Purnama*

Physics Department, Universitas Sebelas Maret, Surakarta 57126, Indonesia

Article history:
Received: 7 August 2024 / Received in revised form: 26 November 2024 / Accepted: 2 December 2024

Abstract

This study details the nickel-substituted cobalt ferrite nanoparticle employing natural fine sediment (NiCFO-fs) annealing temperature dependency of crystalline and magnetic characteristics. The NiCFO-fs nanoparticles were prepared by the coprecipitation method with varying annealing temperatures (200-500°C with increment of 100°C for five hours). As a comparison, Ni-CFO was also synthesized using pure analytical chemicals (NiCFO-pa). The XRD results showed that the whole Ni-CFO nanoparticles established an inverse spinel face center cubic (fcc) order according to space group Fd-3m for both NiCFO-fs and NiCFO-pa. There was no additional peak, indicating that Ni^{2+} cations successfully substituted in cobalt ferrite nanoparticles. In case of NiCFO-fs nanoparticle samples, a crystallite size (D) decreased with the increasing annealing temperature (Ta), namely 45.72 nm, 37.35 nm, 25.95 nm, and 20.51 nm. In contrast to NiCFO-pa, the D increased with the increase of the Ta, i.e., 19.67 nm, 20.74 nm, 21.99 nm, and 23.33 nm. Meanwhile, FTIR results showed the presence of metal-oxygen bonds at 551-586 cm^{-1} and 384-391 cm^{-1} at tetrahedral (k_1) and the octahedral (k_2) sites for both NiCFO-fs and NiCFO-pa nanoparticles samples. The VSM result showed that a narrow hysteresis curve was observed for the NiCFO-fs sample compared to NiCFO-pa. The NiCFO-fs nanoparticles owing the smallest coercive field (H_C) of 79.5 Oe were attained for the Ta of 300°C. In case of NiCFO-fs samples, magnetization saturation (M_S) decreased with the increase of the Ta in contrast to NiCFO-pa samples. Here, the redistribution of two and three plus ions in the sub-lattice k_1 and k_2 locations should be encouraged by the Jahn-Teller phenomenon through strain-induced magnetism. The findings of the antibacterial test indicated that the potential of NiCFO based on natural materials (fine sediment) was higher than that of NiCFO based on pure analytical chemicals. This result was also supported by the emergence of ZOI magnitudes for all NiCFO-fs materials compared to NiCFO-pa that was only at Ta = 300°C.

Keywords: Nanoparticles; cobalt ferrite; nickel; fine sediment

1. Introduction

Cobalt ferrite-based nanoparticles have become an interesting topic since the last decade. The ease of modifying physical characteristics by adjusting the composition [1,2], synthesis [3,4], and annealing temperature [5–7], makes cobalt ferrite-based nanoparticles magnetic a major topic. Moreover, these nanoparticles have wide potential applications due to their unique magnetic, electrical, and optical properties; such as gas sensor [8], photocatalysts [9–11], magneto-rheology [12,13], or antibacterial [14,15].

Theoretically, cobalt ferrite is categorized as an inverse spinel ferrite with trivalent ions dominating tetrahedral sites (A) and divalent ions inhabiting octahedral sites (B). Cobalt ferrite, which is a member of the Fd3m space group, has configuration in which 8 cations occupy tetrahedral sites and 16 occupy octahedral sites, while 64 tetrahedral and 32 octahedral sites are available, respectively [16,17]. Thus, artificially the tetrahedral site is only one-eighth full and half the octahedral site. This provides an opportunity to modify the crystalline features and magnetic behavior of cobalt ferrite-based nanoparticles by substitution of other metal cations, one of which is nickel.

According to several studies, cobalt ferrite nanoparticles that have Ni cations substituted for them have a lower coercive field [1,18–22]. However, selecting a synthesis technique is an additional factor that has to be considered. The coercive field (H_C) was shown to decrease with increasing annealing temperature (Ta) in the case of nickel-substituted cobalt ferrite nanoparticles manufactured in a single step via solvothermal manufacturing. [23]. On the contrary, for sol gel procedure, the H_C of cobalt ferrite nanoparticles with a nickel substitution increased with the increase in the Ta [5]. It has also been

* Corresponding author.
Email: bpurnama@mipa.uns.ac.id
https://doi.org/10.21924/cst.9.2.2024.1495

reported that the use of fine sediment as a source of Fe^{3+} cation in coprecipitated cobalt ferrite nanoparticles may reduce the H_C of 113 Oe [24] and furthermore reduce to 100 Oe in lanthanum substituted cobalt ferrite nanoparticles [25]. This encourages the combination with nickel substitution to further reduce the H_C magnitude; as a result, superparamagnetic will be realized close to room temperature. Superparamagnetic characteristics play a crucial role in the development of antibacterials due to their small H_C and moderate saturation magnetization (M_S) values. This then makes the antibacterial application of Ni-substituted cobalt ferrite nanoparticles a challenge. Only a few papers report the antibacterial performance of nickel substitute cobalt ferrite [26,27]. Fine sediment is a more cost-effective option for the production of cobalt ferrite due to its abundance in nature. Due to the little amount needed, the usage of fine sediment also does not harm the ecosystem. Furthermore, when using a fine sediment source for the synthesis of cobalt ferrite, the coprecipitation technique is one of the keys to the success as shown in several earlier studies [7,12,24,25]. For this reason, this method was chosen for this inquiry above others.

In this paper, the effects of altering the annealing temperature, *T*a, on nickel substituted cobalt ferrite nanoparticles with natural-fine-sediment (NiCFO-fs) sources were analyzed in terms of their crystalline and magnetic characteristics. In laboratory standards, nickel substituted cobalt ferrite nanoparticles were also synthesized using pure analyst chemicals (NiCFO-pa). The resulting nanoparticle samples were subjected to x-ray diffractometer (XRD) and Fourier transform infrared (FTIR) spectroscopy to assess their structural features. Lastly, a room-temperature vibrating sample magnetometer (VSM) was used to measure the magnetic characteristics. In this case, to ascertain their potential in the biomedical arena, the antibacterial activity of both NiCFO-fs and NiCFO-pa nanoparticles was examined.

2. Materials and Methods

Nanoparticle samples of $Ni_xCo_{1-x}Fe_2O_4$ with x=0.06 (NiCFO); were synthesized by coprecipitation route following steps procedure as depicted in schematic diagram of Fig 1. First, stoichiometry quantities of $Ni(NO_3)_2.6H_2O$ (Merck), $Co(NO_3)_2.6H_2O$ (Merck), and fine sediment from Bengawan Solo iron sand were combined with 200 ml of bi-distilled water, and the mixture was agitated for 20 minutes at 300 rpm using a magnetic stirrer until it became homogenous. Subsequently, 100 ml of 4.8 M NaOH solution was gradually added, and the mixture was agitated at 300 rpm with a magnetic stirrer while being kept at 95°C. It was then continued by conducting deposition, which involved washing with ethanol and distilled water. The precipitate originated was dried up in an oven at 100°C for a whole night, and crushed using a mortar and pestle (the obtained product was NiCFO-fs). In laboratory standards, the nanoparticles of NiCFO using standard pure analyst chemicals (NiCFO-pa) were also synthesized using a similar procedure. Furthermore, the NiCFO-fs and NiCFO-pa underwent five hours of annealing at 200°C, 300°C, 400°C, and 500°C.

The crystalline structure of the produced nanoparticles was assessed using x-ray diffractometer (XRD) machine (Bruker D8 Advance system) utilizing Cu $K\alpha_1$ (λ = 1.5406 Å) radiation. Based upon the highest peak of its XRD pattern, the Scherrer equation (D = 0.9 $\lambda/(\beta \cos\theta)$) was used to determine the crystallite size, D. The X-ray radiation's wavelength, λ, the Bragg angle, θ, and the strongest peak's complete breadth at half its greatest height, β, were all given in the equation.

The Stokes-Wilson equation, $\varepsilon = \beta_{hkl}/4\tan\theta$, was used to quantify the change in crystalline strain, ε, caused by the post-annealing treatment. The formula for predicting the lattice constant, a, is $a = \frac{\lambda}{2\sin\theta}\sqrt{h^2+k^2+l^2}$ where h, k, and l are the Miller indexes. The formula $d_x = (Z \cdot M)/(N_A \cdot a^3)$ was used to compute the crystalline density, d_x where Z is the number of formula units per unit cell, M is the molecular weight and N_A is Avogadro's number [25].

The functional groups in the wavenumber k choice of 350–4000 cm^{-1} were identified using Fourier transform infrared spectroscopy (FTIR, Shimadzu IF Prestige 21). The force constant equation in both tetrahedral ($k_t = 7.62 \times M_1 \times v_1^2 \times 10^{-7}$ N/m) and octahedral ($k_o = 10.62 \times M_1/2 \times v_2^2 \times 10^{-7}$ N/m) forms was further employed to determine the shift in the average value of the force constant ($\bar{k}$) in the NiCFO-fs and NiCFO-pa using the equation $\bar{k} = \frac{2k_o + k_t}{3}$, where M_1 and M_2 are the cation's molecular weights at the tetrahedral and octahedral positions, respectively [28,29]. Additionally, the following equation may be used to determine the shifts in Young's modulus E using the FTIR findings and accounting for the

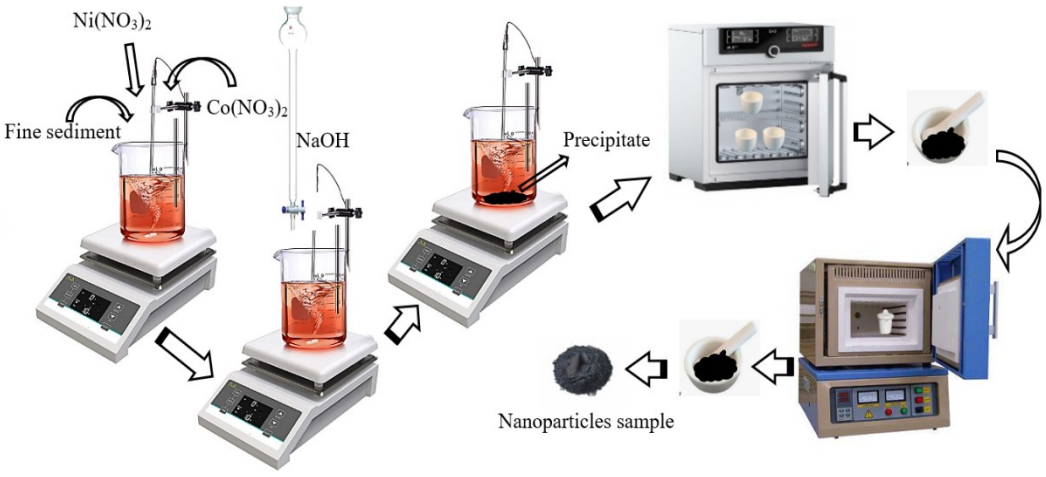

Fig. 1. Diagram flow for synthesizing NiCFO-fs, and NiCFO-pa nanoparticles using coprecipitation routes

elastic stiffness constant and the average force constant [29], $E = \frac{(C_{11}-C_{12})(C_{11}+2C_{12})}{(C_{11}+C_{12})}$ which $\bar{F} = \frac{(2F_0+F_t)}{3}$, $C_{11} = \frac{\bar{F}}{a}$ and $C_{12} = \frac{\delta_P C_{11}}{1-\delta}$. where $\bar{F}$ is the average force constant, C_{11} and C_{12} are the stiffness constants, δ_P is the Poisson's ratio, determined by applying the formula δ_P = 0.324(1-1.043P) (P represents the pore fraction) [30], and E is Young's modulus. In the end, using a VSM (OXFORD VSM 1.2H) at room temperature, the magnetic characteristics were identified. The magnitude of K_σ was calculated as follows, $K_\sigma = \frac{3}{2}\lambda\sigma = \frac{3}{2}\lambda E\varepsilon$ where, λ represents the mean magnetostriction constant ($\lambda = (2\lambda_{100} + 3\lambda_{111})/5$). The pristine cobalt ferrite has two magneto-strictive strain coefficients, i.e., $\lambda_{100} = -5.9 \times 10^{-4}$ and $\lambda_{111} = 1.2 \times 10^{-4}$ along the crystallographic axes <100> and <111> [31].

3. Results and Discussion

Fig.2 depicts the annealing temperatures *T*a (200°C, 300°C, 400°C, and 500°C for 5 hours under atmospheric conditions) modifying the XRD patterns in NiCFO-fs and NiCFO-pa nanoparticles. Both x-ray diffraction patterns, i.e. *hkl* planes (220), (311), (222), (400), (422), (511), and (440) were closely resembled the International Center for Diffraction Data (ICCD) number 221086, which belongs to the face-centered cubic spinel type (Fd-3m) i.e., owing crystalline structure of pristine cobalt ferrite [32]. In addition, the highest *hkl* peak (311) was used as a calculation in obtaining crystalline parameters. Here, there were no distinctive peaks in the NiCFO-pa sample that would have suggested the presence of unexpected oxides or other contaminants. Unfortunately, in the case of the NiCFO-fs nanoparticles, an undesirable peak appeared at an angle of around 25° that was suggested to represent iron oxide. This was because the NiCFO-fs nanoparticle formation reaction competed with the realization of iron oxide from the abundance of Fe^{3+} cations from the fine sediment. Table 1 presents the tabulation of the modifies in crystalline parameters including crystallite size (*D*), lattice constant parameter (*a*), lattice strain (ε), and crystalline density (d_x) due to annealing temperature (i.e. 200°C, 300°C, 400°C, and 500°C for 5 hours) for both nanoparticle samples of NiCFO-fs and NiCFO-pa.

As clearly observed in Table 1, the *D* (45.72 nm, 37.35 nm, 25.95 nm and 20.51 nm) decreased for NiCFO-fs nanoparticles with increasing *T*a (200°C, 300°C, 400°C, and 500°C). On the contrary, the *D* (19.67 nm, 20.74, 21.99 and 23.34 nm) increased with increasing *T*a for NiCFO-fs nanoparticles. Here, there were more indications of competition between undesired of iron oxide and NiCFO-fs nanoparticles production. Changing these *D* in both NiCFO-fs and NiCFO-pa nanoparticles might modify their lattice strain, ε, magnitude. In the case of NiCFO-fs, the *D* decrease of 55.14% (=(45.72-20.51)/45.72) induced to rise in the ε of 54.95% (=(5.55-2.5)/5.55). In contrast to NiCFO-pa, the *D* increase of 15.72% (=(23.34-19.67)/23.34) assisted to a reduce in the ε magnitude of 27.53% (=(5.74-4.160/5.74). These changes in the ε might be used to tune their magnetic properties. It was expected that the changes in magnetic properties should be opposite to each other for the case of NiCFO-fs and NiCFO-pa samples, respectively. Thus, the lattice parameters, *a*, and the crystalline density, d_x, were not sensitive to changes in the *T*a for both NiCFO-fs and NiCFO-pa.

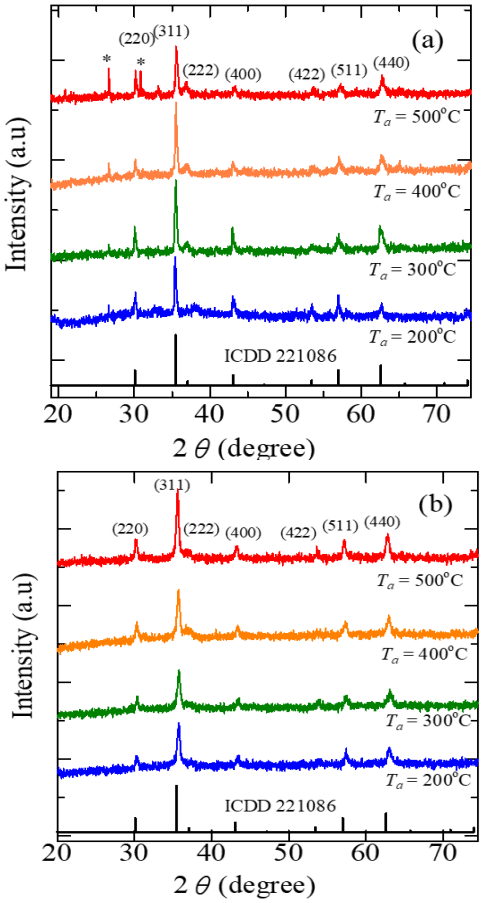

Fig. 2. The XRD pattern of (a) NiCFO-fs and (b) NiCFO-pa nanoparticles annealed at temperatures of 200°C, 300°C, 400°C, and 500°C for 5 hours

Table 1. The calculation of crystallite size (*D*), lattice constant parameter (*a*), lattice strain (ε), and crystalline density (d_x) for NiCFO-fs and NiCFO-pa nanoparticles annealed at temperatures of 200°C, 300°C, 400°C, and 500°C for 5 hours

NiCFO-fs nanoparticles				
*T*a (°C)	*D* (nm)	*a* (Å)	ε (10^{-3})	d_x (g/cm^3)
200	45.72	8.41	2.50	5.23
300	37.35	8.39	3.05	5.27
400	25.95	8.39	4.39	5.28
500	20.51	8.39	5.55	5.28
NiCFO-pa nanoparticles				
200	19.67	8.32	5.74	5.41
300	20.74	8.33	5.45	5.39
400	21.99	8.35	4.87	5.35
500	23.34	8.36	4.16	5.32

Fig. 3 shows the FTIR curve of NiCFO-fs and NiCFO-pa nanoparticles synthesized at T_a of 200°C, 300°C, 400°C and 500°C for 5 hours at an atmospheric condition. Table 2 provides the absorption wave numbers *k* and the calculation of force constants in both octahedral k_o and tetrahedral sites k_t. All samples had several absorption peaks of the FTIR curve, related to hydroxyl bonds, especially NiCFO-fs. Absorption peaks at around 3400 cm^{-1} and 1358 cm^{-1} corresponded to the stretching and bending vibrations of the hydroxyl (OH) group, respectively. The observed absorption peak indicated that the results of the washing process with ethanol, containing hydroxyl groups, were not optimal yet. The variety of the T_a affected the existence of various functional groups. The typical

peak absorption appeared at k ~600 cm^{-1} and around 400 cm^{-1} are the common featured of spinel ferrite and are related to M–O bond stretching at the tetrahedral sites and octahedral, respectively [5,14]. A few shifts in wave number (k_1 and k_2) due to the increase of T_a indicated the change in the force constant of the relating bonds constant. It was reflected in the modify of lattice strain as the previous discussion. It was clearly observed that F increased with increasing annealing temperature for both NiCFO-fs and NiCFO-pa nanoparticles. These results indicated that there was a redistribution of cations at the octahedral and tetrahedral sites. This would appear in the observation of the magnetic properties to be discussed later.

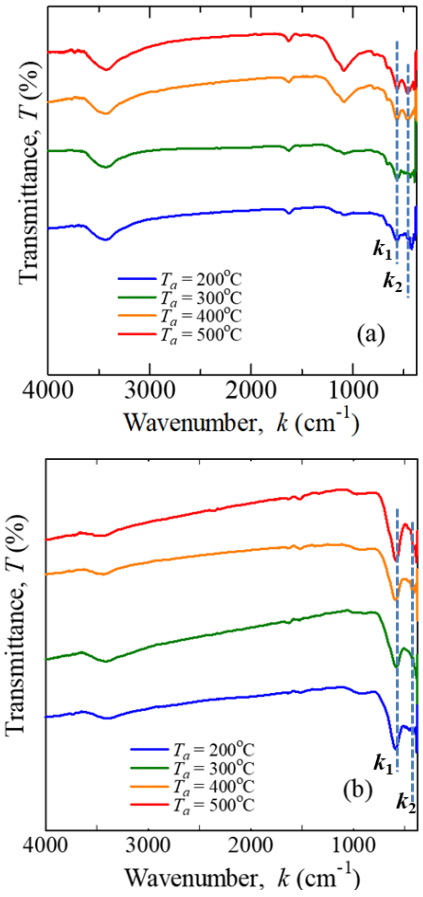

Fig. 3. FTIR pattern of NiCFO-fs and NiCFO-pa nanoparticle with different temperature annealing of 200°C, 300°C, 400°C, and 500°C for 5 hours

Fig. 4 shows the hysteresis curves for (a) NiCFO-fs and (b) NiCFO-pa nanoparticles prepared using co-precipitation methods and individually annealed at T_a = 200°C, 300°C, 400°C and 500°C for 5h. The magnetic parameters as well as the calculation of the strain anisotropy are summarized in Table 3. The calculation of the E and the K_σ carried out was similar to the previous procedure [2,29,31]. It was observed from the curve that narrow hysteresis loop realized of the NiCFO-fs nanoparticles for the whole annealing temperature T_a. Figure 4 shows the hysteresis curves for (a) NiCFO-fs and (b) NiCFO-pa nanoparticles prepared using co-precipitation methods and individually annealed at T_a = 200°C, 300°C, 400°C and 500°C for 5h.

In the case of NiCFO-fs, the smallest coercive field H_C of 79.5 Oe was obtained for the T_a of 300°C. In contrast, a relatively wide of hysteresis curve realized for the whole NiCFO-pa nanoparticles and the largest H_C of 1150 Oe was obtained for sample annealed of 200°C. Meanwhile, The M_S showed a number of different changes between NiCFO-fs and NiFCO-pa nanoparticles. In the case of NiCFO-fs nanoparticles, increasing the T_a from 200°C to 500°C, the M_S magnitude dropped from 30.25 emu/g to 19.81 emu/g (down 34.51% (= (30.25-19.81)/30.25)). Meanwhile for NiCFO-pa, the M_S rose with the increase in the T_a i.e., 18.72 emu/g at T_a of 200°C to 38.53 emu/g (up 51.41% (= (38.53-18.72)/38.53)) at T_a of 500°C. To explain this interesting phenomenon, the changes in Young's modulus E of NiCFO-fs and NiCFO-pa nanoparticles were evaluated, respectively. The calculated E value increased with the increase of the T_a for sequence nanoparticle sample. Furthermore, to determine the effect of induced lattice strains on each sample, constant magnetoelastic anisotropy K_σ calculations were carried out. The results were found very interesting; for the NiCFO-fs sample, K_σ increased with increasing annealing temperature from 6.81×10^4 erg/cm^3 to 16.89 ×10^4 erg/cm^3 (the change of + 10.08×10^4 erg/cm^3). This is consistent with earlier studies [5]. In contrast, for the NiCFO-pa nanoparticles sample, there was a decrease from 15.27×10^4 erg/cm^3 to 14.08 ×10^4 erg/cm^3 (the change of –1.19×10^4 erg/cm^3). If the Jahn-Teller effect due to the strain-induced magnetoelastic anisotropy constant was considered, then the change in the K_σ showed the occurrence of cation redistribution at octahedral and tetrahedral sites. As known, the total magnetic moment in the fcc inverse spinel crystal structure is the difference between the magnetic moment at the

Table 2. The absorption band and force constant calculation at the tetrahedral *(k1)* and octahedral *(k2)* sites for NiCFO-fs and NiCFO-pa nanoparticle with different temperature annealing of 200°C, 300°C, 400°C, and 500°C for 5 hours.

T_a (°C)	k_1 (cm^{-1})	k_2 (cm^{-1})	Force constant (N/m)		
			Tetrahedral site k_t	Octahedral site k_o	Average F
NiCFO-fs					
200	512.12	391.57	111.97	96.16	101.43
300	564.20	392.53	135.90	96.63	107.52
400	566.13	384.82	136.83	92.87	109.72
500	562.27	398.92	134.97	99.50	111.32
NiCFO-pa					
200	586.39	369.38	146.80	85.55	105.97
300	581.56	373.24	144.39	87.35	106.36
400	592.17	387.71	149.71	94.25	112.74
500	585.42	406.03	146.32	103.37	117.69

octahedral site occupied by divalent cations and the magnetic moment at the tetrahedral site where divalent and trivalent cations occupy [33–35]. The calculation results showed that if the change in the K_σ was positive, then the divalent cations in the octahedral site allowed to migrate to the tetrahedral site. As a result, the net magnetic moment decreased as appeared by the decreasing value of *MS*. In contrast, if the K_σ change was negative, the divalent cation promoted moves from the tetrahedral to the octahedral site within result the M_S increases with an increase in the T_a.

Fig. 5 shows the antibacterial performance of the (a,b) NiCFO-fs and (c,d) NiCFO-pa nanoparticles with different temperature annealing for *E.coli* and *S. Aureus* bacteria, which appeared as the zone of inhibition (ZOI). Table 4 presents the summary of the ZOI calculation for individual sampling. In case for NiCFO-fs nanoparticles as antibacterial agent, the ZOI was clearly observed for both *E. coli* and *S. aureus*. The largest of the ZOI of 14.48 mm was obtained for NiCFO-fs nanoparticles sample with annealing at 500°C in *E. coli* bacteria. Here, the performance antibacterial was 47.47%(=(30.50-14.48)/30.50) in comparison to standard. While, for *S.aureus* bacteria, the ZOI of 13.02 mm (49.28%) was obtained for NiCFO-fs nanoparticles sample with annealing at 200°C. If particle size was discussed as a

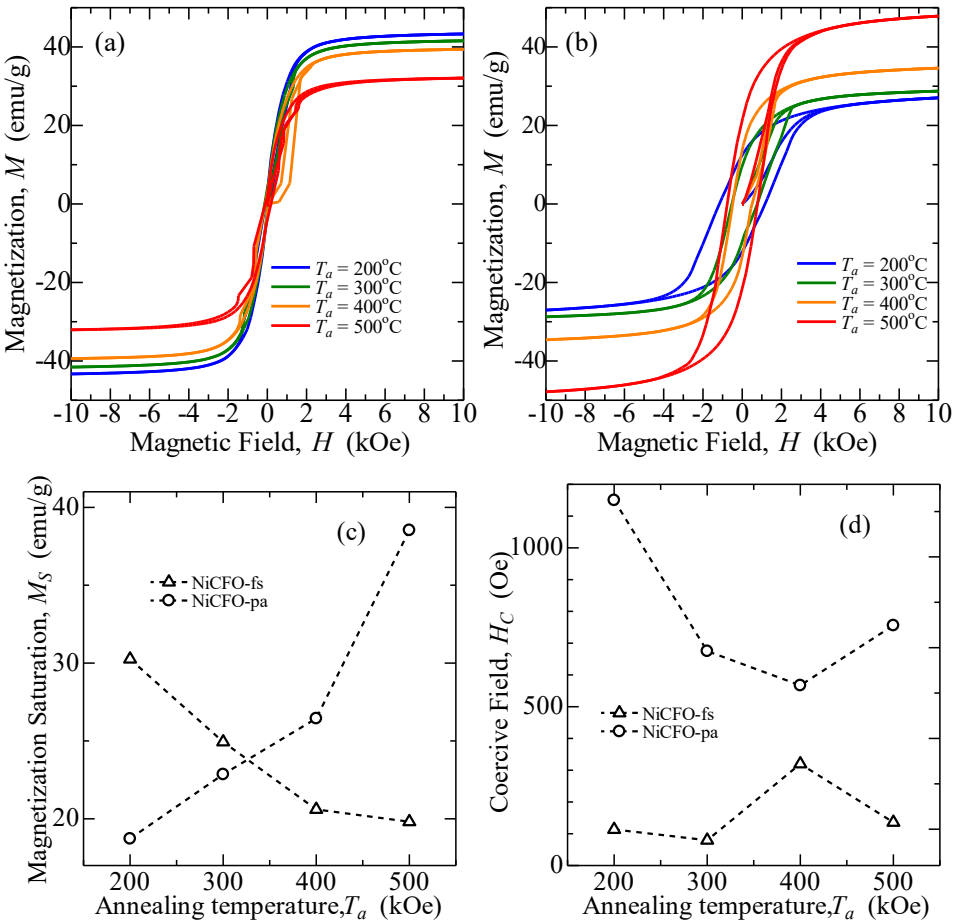

Fig. 4. The M-H hysteresis curve of (a) NiCFO-fs and (b) NiCFO-pa nanoparticle with different temperature annealing T_a of 200°C, 300°C, 400°C, and 500°C for 5 hours. (c) The magnetization saturation M_S and (d) the coercive field H_C as a function as temperature annealing T_a.

Table 3. Calculation of Young's modulus *E*, magnetoelastic anisotropy constant $K\sigma$, coercive field *HC* and saturation magnetization *MS* in (a) NiCFO-fs and (b) NiCFO-pa nanoparticles with 5 hours annealed of 200°C, 300°C, 400°C, and 500°C.

Ta(°C)	E ($\times 10^{10}$ N/m^2)	K_σ ($\times 10^4$ erg/cm^3)	*H*c (Oe)	*M*s (emu/g)
NiCFO-fs				
200	11.35	6.81	113.41	30.25
300	11.45	8.38	79.50	24.94
400	12.14	12.79	319.83	20.60
500	12.68	16.89	135.92	19.81
NiCFO-pa				
200	11.08	15.27	1150.01	18.72
300	11.96	15.64	675.24	22.86
400	11.67	11.65	567.31	26.44
500	12.04	14.08	756.26	38.53

determining factor in antibacterial performance, small particle size was effective as an antibacterial agent for *S.aureus*, and vice versa for E.coli. The magnetization saturation should expect support the antibacterial mechanism. This also supports earlier research that highlighted a correlation between variations in antibacterial activity and variations in saturation magnetization [36,37]. Contrastively, it was only for the NiCFO-pa nanoparticles with annealing temperature of 300°C indicating as an antibacterial agent for both *S.aureus* and *E.Coli*, NiCFO-fs exhibited full antibacterial activity due to its superparamagnetic characteristics (Fig. 4). The results obtained (ZOI = around 11-14 mm) also had slightly better activity than previous studies, where the ZOI magnitude for MCFO (M=Zn, Ni, Ag, Cu) was around 7-13 mm [14,36,38]. This explains that the potential for antibacterial development is still very open by using fine sediment as a source of cobalt ferrite nanoparticle material.

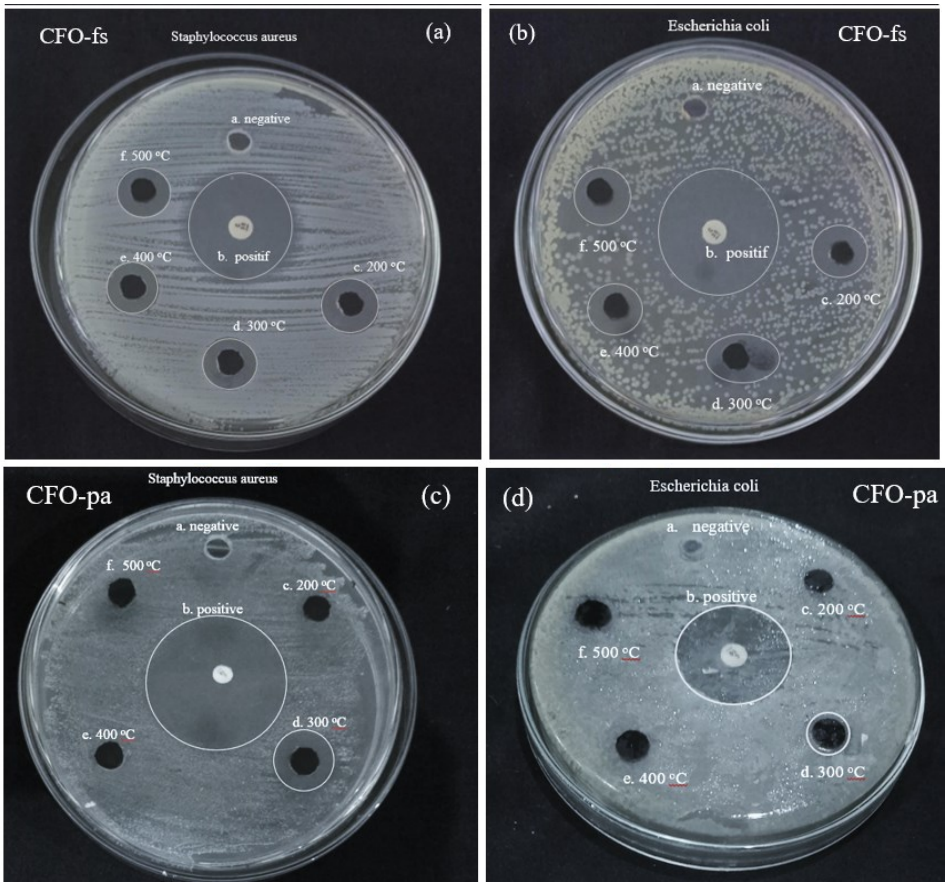

Fig. 5. the ZOI of (a,b) NiCFO-fs and (c,d) NiCFO-pa nanoparticle with different temperature annealing T_a of 200°C, 300°C, 400°C, and 500°C for 5 hours for E.coli and S.aureus bacteri

Table 4. The comparison of the Zone of Inhibition (ZOI) calculation in NiCFO-fs and NiCFO-pa nanoparticles with 5 hours annealed of 200°C, 300°C, 400°C, and 500°C

Ta (°C)	ZOI (mm)			
	NiCFO-fs		NiCFO-pa	
	E.coli	S.aureus	E.coli	S.aureus
+ control	30.50	26.42	22.44	51.44
– control	0	0	-	-
200	14.02	13.02	0	0
300	14.10	11.82	18.01	37.01
400	13.24	11.93	0	0
500	14.48	11.79	0	0

4. Conclusions

Nanoparticle samples Annealing temperature dependence of structural and magnetic properties in nickel substituted cobalt ferrite nanoparticles using natural-fine-sediment (NiCFO-fs) is presented. The NiCFO-fs nanoparticles were prepared by the coprecipitation method with various annealing temperatures of 200°C, 300°C, 400°C, and 500°C for 5 hours. As a comparison, Ni-CFO was also synthesized using pure analytical chemicals (NiCFO-pa).

The XRD results showed that the whole Ni-CFO nanoparticles had an inverse spinel face center cubic (fcc)

structure according to space group Fd-3m for both NiCFO-fs and NiCFO-pa. There was no addition peak, indicating that Ni^{2+} cations successfully substituted in cobalt ferrite nanoparticles. In the case of NiCFO-fs nanoparticle samples, a crystallite size (D) decreased with the increase of the annealing temperature (Ta), namely 45.72 nm, 37.35 nm, 25.95 nm, and 20.51 nm. In contrast to NiCFO-pa, the D increased with the increase of the Ta, i.e., 19.67 nm, 20.74 nm, 21.99 nm, and 23.33 nm. FTIR results showed the presence of metal-oxygen bonds at 551 cm^{-1}-586 cm^{-1} and 384 cm^{-1}-391 cm^{-1} at tetrahedral (k_1) and the octahedral (k_2) sites for both NiCFO-fs and NiCFO-pa nanoparticles samples.

The VSM result showed that a narrow hysteresis curve was observed for the NiCFO-fs sample compared to NiCFO-pa. The NiCFO-fs nanoparticles owing the smallest coercive field H_C of 79.5 Oe were attained for the Ta of 300°C. In the case of NiCFO-fs samples, magnetization saturation M_S decreased with the increase of the Ta in contrast to NiCFO-pa samples. Here, the Jahn-Teller effect via strain-induced magnetism should promote a redistribution of both divalent and trivalent cations in the octahedral and the tetrahedral sites. The results of the antibarial test showed that NiCFO based on fine sediment had a higher potential than NiCFO based on pure analytical chemicals. The appearance of ZOI magnitudes for all NiCFO-fs materials in comparison to NiCFO-pa, which was only present at Ta = 300°C, can support this conclusion. Hence, this will lead to a deeper investigation of cobalt ferrite nanoparticles in the future, particularly in the biomedical field, employing natural material sources (fine sediment).

5. Acknowledgments

This study was financially supported by Penelitian Hibah Grup Riset (Penelitian HGR UNS A) Universitas Sebelas Maret, Indonesia contract number: 194.2/UN27.22/PT.01.03/2024.

References

1. P.A. Vinosha, A. Manikandan, R. Ragu, A. Dinesh, K. Thanrasu, Y. Slimani, A. Baykal, B. Xavier, *Impact of nickel substitution on structure, magneto-optical, electrical and acoustical properties of cobalt ferrite nanoparticles*, J. Alloys Compd. 857 (2021) 157517.
2. N.P. Prasetya, R.I. Setiyani, Utari, K. Kusumandari, Y. Iriani, J. Safani, A. Taufiq, N.A. Wibowo, S. Suharno, B. Purnama, *Cation trivalent tune of crystalline structure and magnetic properties in coprecipitated cobalt ferrite nanoparticles*, Mater. Res. Express. 10 (2023).
3. A. Sharifi, R. Hayati, N. Setoudeh, G. Rezaei, *A comparison between structural and magnetic behavior of cobalt ferrite synthesized via solid state and chemical methods*, Mater. Res. Express. 8 (2021).
4. M.A. Albalah, Y.A. Alsabah, D.E. Mustafa, *Characteristics of co-precipitation synthesized cobalt nanoferrites and their potential in industrial wastewater treatment*, SN Appl. Sci. 2 (2020) 1–9.
5. S. Budiawanti, R. Amalia, D.T. Rahardjo, Suharno, B. Purnama, D. Djuhana, *Influences of Postannealing Treatment Parameters on the Structural and Magnetic Properties of Nickel-Doped Cobalt Ferrite Synthesized by Sol-Gel Route*, J. Magn. 27 (2022) 88–95.
6. A.H. Omran Alkhayatt, S.K. Muhammad, A.A. Habieb, A.H. Ali, S.H. Mohsen, R.R. Munem, *Low annealing temperature effect on Structural, and optical properties of CuO nanostructure thin films*, IOP Conf. Ser. Mater. Sci. Eng. 871 (2020).
7. N.P. Prasetya, Utari, Y. Iriani, B. Purnama, *The Effect of Annealing Temperature on the Structural and Magnetic Properties of Lanthanum Doped Cobalt Ferrite with the Bengawan Solo River Fine Sediment as the Source of Fe3+*, Key Eng. Mater. 940 (2023) 11–20.
8. S. Joshi, V.B. Kamble, M. Kumar, A.M. Umarji, G. Srivastava, *Nickel substitution induced effects on gas sensing properties of cobalt ferrite nanoparticles*, J. Alloys Compd. 654 (2016).
9. C. Singh, A. Goyal, S. Singhal, *Nickel-doped cobalt ferrite nanoparticles: Efficient catalysts for the reduction of nitroaromatic compounds and photo-oxidative degradation of toxic dyes*, Nanoscale. 6 (2014).
10. M.M. Naik, H.S.B. Naik, N. Kottam, M. Vinuth, G. Nagaraju, M.C. Prabhakara, *Multifunctional properties of microwave-assisted bioengineered nickel doped cobalt ferrite nanoparticles*, J. Sol-Gel Sci. Technol. 91 (2019).
11. J. Revathi, M.J. Abel, V. Archana, T. Sumithra, R. Thiruneelakandan, J. Joseph prince, *Synthesis and characterization of CoFe2O4 and Ni-doped CoFe2O4 nanoparticles by chemical Co-precipitation technique for photo-degradation of organic dyestuffs under direct sunlight*, Phys. B Condens. Matter. 587 (2020).
12. K.C. Nugroho, Ubaidillah, B. Purnama, A. Mas'udi, N.A. Nordin, S.A. Mazlan, S.B. Choi, *The effect of MnxCo(1-x)Fe2O4 with x = 0, 0.25 and 0.5 as nanoparticles additives in magnethorheological fluid*, Smart Mater. Struct. 29 (2020).
13. K.C. Nugroho, U. Ubaidillah, R. Arilasita, M. Margono, B.H. Priyambodo, B. Purnama, S.A. Mazlan, S.B. Choi, *The effect of Sr-CoFe2O4 nanoparticles with different particles sized as additives in CIP-based magnetorheological fluid*, Materials (Basel). 14 (2021).
14. G. Rajivgandhi, G. Ramachandran, G. Chackaravarthi, C.K. Chelliah, M. Maruthupandy, F. Quero, F.A. AL-mekhlafi, M.A. Wadaan, W.J. Li, *Preparation of antibacterial Zn and Ni substituted cobalt ferrite nanoparticles for efficient biofilm eradication*, Anal. Biochem. 653 (2022).
15. S. Sundram, S. Baskar, A. Subramanian, *Green synthesized nickel doped cobalt ferrite nanoparticles exhibit antibacterial activity and induce reactive oxygen species mediated apoptosis in MCF-7 breast cancer cells through inhibition of PI3K/Akt/mTOR pathway*, Environ. Toxicol. 37 (2022).
16. R.K. Kotnala, J. Shah, *Ferrite Materials*, in: BS:HMM, Elsevier, 2015: pp. 291–379.
17. M. Fantauzzi, F. Secci, M. Sanna Angotzi, C. Passiu, C. Cannas, A. Rossi, *Nanostructured spinel cobalt ferrites: Fe and Co chemical state, cation distribution and size effects by X-ray photoelectron spectroscopy*, RSC Adv. 9 (2019) 19171–19179.
18. M. Mozaffari, J. Amighian, E. Darsheshdar, *Magnetic and structural studies of nickel-substituted cobalt ferrite nanoparticles, synthesized by the sol-gel method*, J. Magn. Magn. Mater. 350 (2014).
19. A. Kumar, N. Yadav, D.S. Rana, P. Kumar, M. Arora, R.P. Pant, *Structural and magnetic studies of the nickel doped CoFe2O4 ferrite nanoparticles synthesized by the chemical co-precipitation method*, J. Magn. Magn. Mater. 394 (2015).
20. U.B. Sontu, V. Yelasani, V.R.R. Musugu, *Structural, electrical and magnetic characteristics of nickel substituted cobalt ferrite nano particles, synthesized by self combustion method*, J. Magn. Magn. Mater. 374 (2015).
21. S. Bhame, M. Shirolkar, P.A. Joy, *Magnetic and Magnetoelastic Properties of Ni-Substituted Cobalt Ferrite*, IEEE Magn. Lett. 12 (2021).
22. R.S. Melo, A. Franco, P. Banerjee, *Nanoscale-driven single-domain structure in nickel substituted superparamagnetic cobalt ferrites*, Solid

State Commun. 341 (2022).

23. G. Datt, M. Sen Bishwas, M. Manivel Raja, A.C. Abhyankar, *Observation of magnetic anomalies in one-step solvothermally synthesized nickel-cobalt ferrite nanoparticles*, Nanoscale. 8 (2016).
24. B. Purnama, A.D. Suwandi, R. Hartono, S.A.T. Bawono, U. Utari, H. Aldila, A. Rahwanto, K. Kusumandari, *Annealing Temperature Dependence on Magnetic Properties, Crystalline Structure and Photocatalyst Activity of Coprecipitated Cobalt Ferrite (CoFe2O4) Synthesised from Natural Iron Sand*, J. Phys. Sci. 34 (2023) 75–89.
25. N.P. Prasetya, Utari, Y. Iriani, B. Purnama, *The Effect of Annealing Temperature on the Structural and Magnetic Properties of Lanthanum Doped Cobalt Ferrite with the Bengawan Solo River Fine Sediment as the Source of Fe3+*, in: Key Eng. Mater., (2023).
26. N. Sanpo, C. C.Berndt, C. Wen, J. Wang, *Transition metal-substituted cobalt ferrite nanoparticles for biomedical applications*, Acta Biomater. 9 (2013) 5830-5837.
27. G. Rajivgandhi et al., *Preparation of antibacterial Zn and Ni substituted cobalt ferrite nanoparticles for efficient biofilm eradication*, Anal. Biochem. 653 (2022) 114787.
28. S. Amiri, H. Shokrollahi, *Magnetic and structural properties of RE doped Co-ferrite (RE=Nd, Eu, and Gd) nano-particles synthesized by co-precipitation*, J. Magn. Magn. Mater. 345 (2013).
29. J.N. Pavan Kumar Chintala, S. Bharadwaj, M. Chaitanya Varma, G.S.V.R.K. Choudary, *Impact of cobalt substitution on cation distribution and elastic properties of Ni–Zn ferrite investigated by X-ray diffraction, infrared spectroscopy, and Mössbauer spectral analysis*, J. Phys. Chem. Solids. 160 (2022).
30. S.S. Bhatu, V.K. Lakhani, A.R. Tanna, N.H. Vasoya, J.U. Buch, P.U. Sharma, U.N. Trivedi, H.H. Joshi, K.B. Modi, *Effect of nickel substitution on structural, infrared and elastic properties of lithium ferrite*, Indian J. Pure Appl. Phys. 45 (2007) 596–608.
31. K. V. Chandekar, K.M. Kant, *Strain induced magnetic anisotropy and 3d7 ions effect in CoFe2O4 nanoplatelets*, Superlattices Microstruct. 111 (2017) 610–627.
32. A. Saremi, S.M. Mirkazemi, A. Sazvar, H. Rezaie, *Ontrolling magnetic and surface properties of cobalt ferrite nanoparticles: A comparison of co-precipitation and solvothermal synthesis methods*, Solid State Sci. 148 (2023) 107432.
33. H. Ghorbani, M. Eshraghi, A.A. Sabouri Dodaran, P. Kameli, *Study on the effects of cadmium and chromium substitution in hydrothermally-synthesized spinel cobalt ferrite nanoparticles*, Eur. Phys. J. Plus. 138 (2023).
34. X. Jing, M. Guo, Z. Li, C. Qin, Z. Chen, Z. Li, H. Gong, *Study on structure and magnetic properties of rare earth doped cobalt ferrite: The influence mechanism of different substitution positions*, Ceram. Int. 49 (2023).
35. Y. Kalyana Lakshmi, S. Bharadwaj, S. Chanda, C. Venkata Koti Reddy, S. Pola, K. V. Siva Kumar, *Iron ion non-stoichiometry and its effect on structural, magnetic and dielectric properties of cobalt ferrites prepared using oxalate precursor method*, Mater. Chem. Phys. 295 (2023).